Chemical Engineering Journal 478 (2023) 147366

Contents lists available at ScienceDirect

Chemical Engineering Journal

journal homepage: www.elsevier.com/locate/cej

Highly flexible multilayer MXene hollow carbon nanofibers confined with Fe_3C particles for high-performance lithium-ion batteries

Xiaohong Lu [a], Jinbing Cheng [a,*], Dawei Zhou [a], Yichong Chen [a], Hao Jiang [a], Yang Lu [b], Deyang Zhang [b], Dezhi Kong [e], Paul K. Chu [d], Hui Ying Yang [c,*], Yongsong Luo [a,b,*]

[a] Henan International Joint Laboratory of MXene Materials Microstructure, College of Physics and Electronic Engineering, Nanyang Normal University, Nanyang 473061, PR China
[b] Key Laboratory of Microelectronics and Energy of Henan Province, Engineering Research Center for MXene Energy Storage Materials of Henan Province, Henan Joint International Research Laboratory of New Energy Storage Technology, Xinyang Normal University, Xinyang 464000, PR China
[c] Pillar of Engineering Product Development, Singapore University of Technology and Design, 8 Somapah Road, 487372 Singapore, Singapore
[d] Department of Physics, Department of Materials Science & Engineering, and Department of Biomedical Engineering, City University of Hong Kong, Tat Chee Avenue, Kowloon, Hong Kong, PR China
[e] Key Laboratory of Material Physics, Ministry of Education, School of Physics and Microelectronics, Zhengzhou University, Zhengzhou 450052, PR China

ARTICLE INFO

Keywords:
MXene fibers
Fe_3C
Electrospinning
Lithium-ion battery
Self-supporting

ABSTRACT

Designing electrode structures with excellent mechanical properties, fast electrochemical kinetics and stability is important for the development of flexible wearable electrodes. In this paper, a hollow carbon nanofiber composite of $Ti_3C_2T_x$ MXene and Fe_3C nanoparticles is designed. The synergistic effect of $Ti_3C_2T_x$ MXene and Fe_3C nanoparticles forms a strong conductive channel with the hollow channel to form a dual conductive channel, which plays an important role in the preparation of high-performance lithium-ion batteries. Benefiting from the advantages of the above structure, the Fe_3C@MXene/hollow multichannel carbon fibers (Fe_3C@MXene/HMCFs) electrodes at a current density of 0.2 A/g achieve an initial capacity of 1294 mA h g^{-1} and a high reversible capacity of 831 mA h g^{-1} after 200 turns of charge/discharge cycles.

1. Introduction

The energy dilemma has been receiving a great deal of attention, and green renewable energy sources such as rechargeable batteries, supercapacitors, photocatalysis, and electrocatalysis are very important [1–3]. To meet the increasing energy demand, there is a great interest in flexible electrode research, including applications in drive devices for wearable electronics, energy harvesting devices for power generation, and wearable antennas for wireless communication [4–6]. Electrode materials play an important role in high-performance energy storage devices, and high specific capacity and stable electrochemical properties have been the focus of research on electrode materials [7,8]. Rechargeable lithium-ion batteries (LIBs) have been receiving attention due to their high energy density and long cycle life. However, the problems of low conductivity and volume expansion of LIBs have also been troubling. In recent years, excellent two-dimensional (2D) conductive materials have been widely investigated, and the incorporation of conductive 2D materials has been demonstrated through several studies to be beneficial for improving electron/ion transport and increasing specific capacity.

In the past few years, extensive research on 2D materials has provided the basis for our understanding of 2D materials. Among the family of 2D materials, transition metal carbides (MXene), a novel material with a layered structure, have received much attention. Due to its large and tunable interlayer space, excellent hydrophilicity, extraordinary conductivity, and rich surface chemistry, has led to the use of $Ti_3C_2T_x$ MXene as an electrode material and in other components of batteries. However, the relatively low capacity of $Ti_3C_2T_x$ MXene limits its application in rechargeable batteries [9–11]. Moreover, $Ti_3C_2T_x$ MXene is susceptible to van der Waals inters tacking, resulting in impaired electrochemical properties. However, $Ti_3C_2T_x$ MXene, with its high electrical conductivity, rich surface chemistry and special two-dimensional structure, has great potential for application and is a good substrate for the preparation of composite electrode materials [12,13]. Therefore,

* Corresponding authors at: Henan International Joint Laboratory of MXene Materials Microstructure, College of Physics and Electronic Engineering, Nanyang Normal University, Nanyang 473061, PR China.
E-mail addresses: chengjinbing1988@163.com (J. Cheng), yanghuiying@sutd.edu.sg (H.Y. Yang), ysluo@xynu.edu.cn (Y. Luo).

https://doi.org/10.1016/j.cej.2023.147366
Received 28 August 2023; Received in revised form 21 October 2023; Accepted 13 November 2023
Available online 16 November 2023

research on high specific capacity has begun to focus on the recombination of $Ti_3C_2T_x$ MXene with other high-capacity materials.

One of the areas of progress is the addition of carbon nanofiber materials to lithium-ion batteries because of their high aspect ratio, high surface area, controllable chemistry, and abundance of composite forms. Carbon nanofibers as an anode material for the preparation of lithium-ion batteries are often used in conjunction with active materials due to their low electrical conductivity [14], and many researchers have worked on constructing advanced fiber materials with electrical conductivity in the past decades. For example, Sun et al. used Ti_3C_2 MXene as an electrode for lithium-ion batteries and obtained a capacity of 126 mAh g^{-1} [15]. Seo et al. then combined MXene with carbon nanofibers to obtain a specific capacity of 334 mAh g^{-1} [16]. Subsequently, Guo et al. designed to combine MXene with transition metal oxides and carbon nanofibers to obtain a specific capacity of 800 mAh g^{-1} [7]. Qiu et al. finally obtained a specific capacity of 406 mAh g^{-1} by combining Co-mof with MXene and carbon nanofibers [17]. These materials have well-designed structures and enhanced electrochemical properties, and their application in lithium-ion batteries can be effectively improved by combining MXene with carbon nanofibers.

Transition metal carbides have low price, excellent chemical properties and good electrocatalytic properties. It may be a promising electrode candidate for LIBs in rechargeable energy storage systems. For example, Zhang et al. obtained a high specific capacity of 858 mA h g^{-1} by designing Fe_3C-FeN heterostructures combined with N-doped carbon frameworks [18], and Jin et al. embedded Fe_3C in ordered micro mesoporous carbon spheres as a cathode material for lithium-sulfur batteries [19]. Some research groups, such as Zhou's, have proposed transition metal nanoparticles can activate the reversible conversion of some solid electrolyte interface (SEI) film components, which further favors the reversible capacity [20–22]. However, when Fe_3C is used as an electrode material, the repeated embedding and withdrawal of Li^+ during the charging and discharging process can cause a large volume expansion of the material, a decrease in the active chemicals, and the problem of decreasing reversible capacity. In order to overcome this problem, many studies have used various methods to prepare Fe_3C composites, including electrostatic spinning, polymerization-pyrolysis, and sol–gel processes. In the present work, the method of introducing Fe_3C nanoparticles in electrostatic spinning was used. The Fe_3C nanoparticles were embedded into the interior of the nanofibers, which triggered the confinement effect of the fibers and ensured their structural integrity during the charge/discharge process [23,24]. Polyacrylonitrile (PAN) carbon precursor improves the conductivity of the electrode material due to its high carbon yield and ease of spinning, while polyacrylonitrile used in the carbon nanofibers prepared by electrostatic spinning can provide a large amount of N source after the stepwise annealing process. The rapid ion/electron transfer was severely hindered because the adhesive blocked the Li^+ diffusion channel [25]. Therefore, the development of stand-alone electrodes has emerged as a promising strategy that can be directly free of any additives and collectors and provide fast ion diffusion and electron transfer pathways throughout the electrode substrate.

Herein, we report a simple preparation of composite Fe_3C@MXene/HMCFs hollow carbon nanofibers by coaxial electrostatic spinning and stepwise annealing. Its unique structural design offers multiple advantages when used as anode for lithium-ion batteries: the confinement effect of carbon nanofibers during the synthesis of $Ti_3C_2T_x$ MXene and Fe_3C nanoparticles can effectively alleviate the buildup of $Ti_3C_2T_x$ MXene and the agglomeration of Fe_3C nanoparticles [26]; synergistic effect of $Ti_3C_2T_x$ MXene and Fe_3C nanoparticles can promote the conductivity and enhance the reaction kinetics; the hollow carbon nanofibers as the matrix are interlaced with each other to form a three-dimensional electron conduction network, which has a large specific surface area and internal hollow structure to provide a large number of active sites for the chemical reaction in the charge/discharge cycle, which establishes a good conductive channel for the rapid diffusion of Li^+ and the transport of electrons/ions, and at the same time, effectively alleviates the problem of volume expansion, which has a greater impact on the electrochemical performance of lithium-ion batteries [27,28]. Therefore, the composite electrode Fe_3C@MXene/HMCFs has higher electrochemical performance, and the average specific capacity is as high as 1100 mA h g^{-1} after 200 cycles at a current density of 0.2 A/g, which is 1.5 times higher than that of Fe_3C/HMCFs electrode, 1.9 times higher than that of MXene/HMCFs electrode, and 2.4 times higher than that of HMCFs electrode.

2. Experimental

As shown in Fig. 1, Fe_3C@MXene/HMCFs have been synthesized through an electrospinning technique followed by stepwise thermal annealing processes. N, N-dimethyformamide, polyacrylonitrile, polymethyl methacrylate, ferric chloride anhydrous, and Ti_3C_2 MXene flakes are the raw materials for the preparation of hollow Fe_3C@MXene/HMCFs. Ti_3C_2 MXene flakes and N, N-dimethylformamide were ultrasonically dispersed in ice water, then ferric chloride anhydrous was added to continue good dispersion, and polyacrylonitrile was added at the end of dispersion and stirred well to form solution a. Poly (methyl methacrylate) was added to N, N-dimethylformamide and a homogeneous inner layer solution was obtained under continuous stir to form solution b. Subsequently, separate syringes were filled with the inner and outer layer solution for coaxial spinning. The flow rate of core and shell solutions were 0.22 and 0.5 mL h^{-1}, respectively. The distance between the spinneret and the receiving roller was 13 cm, and the voltage was 27 kV. Finally, the as-collected nanofibers were first dewatered at a temperature of 60 ℃ in the air for 6 h and the fibers were heat-treated at 250 °C for 125 min (2 °C min^{-1}) under air and carbonized at 700 ℃ for 70 min (10 °C min^{-1}) under N_2. The anhydrous ferric trichloride reacts with water in N, N-dimethylformamide solution to form iron hydroxide, which finally becomes iron carbide during carbonization to obtain Fe_3C@MXene/HMCFs. The Fe_3C/HMCFs, HMCFs and MXene/HMCFs were also obtained using a similar method.

2.1. Material characterization

Samples were scanned using X-ray diffractometer (XRD, Rigaku D/texultra 250) in the 2-Theta Angle range of 5°-80°, and the crystal structure and phase purity were analyzed using A Cu-Ka ($\lambda = 1.5418$ Å) radiation source. A Raman microprobe (Renishaw instrument) 532 nm Raman laser source broker and a 50x objective lens of India Raman microprobe lens were used for the Raman. The chemical composition and functional groups on the surface of composite materials were analyzed using X-ray photoelectron spectroscopy (XPS, K-ALPHA 0.5 eV,

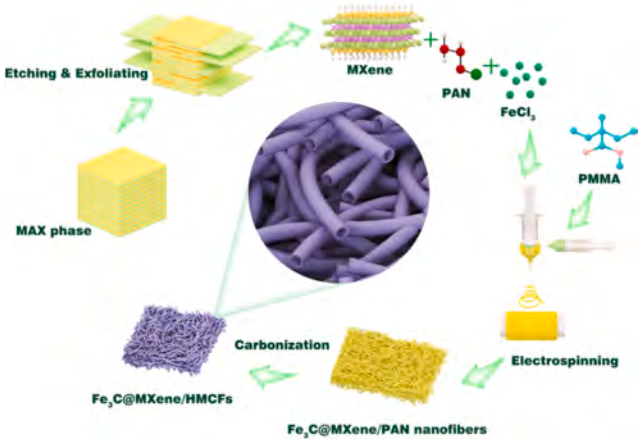

Fig. 1. Schematic diagram of the multi-step preparation process of Fe_3C@MXene/HMCFs nanocomposite.

Thermo Scientific, USA). The morphology and structure of composite material samples were tested using field emission scanning electron microscopy (FESEM, S-4800, Hitachi, Japan) and transmission electron microscopy (TEM, Tecnai G2 F20, FEI, USA). Elemental analysis was performed using an energy dispersive X-ray spectrometer (Bruker-QUANTAX).

2.2. Electrochemical measurements

The prepared Fe_3C/HMCFs, MXene/HMCFs and Fe_3C@MXene/HMCFs were cut into small discs with diameters ca 16 mm and used as cathode directly without any additives. Standard 2032 type coin cells were assembled in an Ar-filled glove box. The electrolyte consisted of 1 M $LiPF_6$ in a solvent of DOL/DME (1:1, V/V). Electrochemical performances (galvanostatic charge–discharge, cycle stability and rate capacity) were tested by LANDIAN (CT3001A). The cyclic voltammetry (CV) with a voltage window of 0.01~3.0 V and electrochemical impedance spectroscopy (EIS) was measured by an electrochemical workstation CH (CHI660E).

3. Results and discussion

Fig. 2**a** shows SEM images of Ti_3AlC_2 with some slight flake textures (~≤10 μm) in field emission scanning electron microscopy (SEM), and Fig. 2**b-c** show photographs of ultrathin Ti_3C_2 flakes obtained by etching of Ti_3AlC_2 using hydrochloric acid and hydrofluoric acid. Fig. 2**d** shows Fe_3C/HMCFs with carbon nanofibers of 400 nm in diameter and relatively fine and straight carbon nanofiber morphology. Fig. 2**g** shows the SEM image of Fe_3C@MXene/HMCFs with curved carbon nanofibers, indicating the successful incorporation of MXene nanosheets. The incorporation of MXene nanosheets can effectively increase the flexibility of carbon nanofibers (Fig. S3). Fig. 2**h** shows the morphology of the carbon nanofibers formed bent and Fe_3C nanoparticles successfully embedded as compared to Fig. 2**e**. The synergistic effect of Fe_3C nanoparticles with MXene promotes electron/ion transport. The hollow pore sizes of the HMCFs in Fig. 2**f** and Fe_3C@MXene/HMCFs in Fig. 2**i** are compared with a pore sizes of about 247 nm. In order to prepare hollow carbon nanofibers with larger pore size to provide more active sites during the charging and discharging of Li-ion batteries as well as to alleviate the volume expansion, we adjusted the size of hollow pore size by adjusting the ratio of PMMA in the core solution several times. As shown in Fig. S4**a**, when the ratio of PMMA:DMF in the core solution is 0.3:1, the hollow pore size is only 60 nm; when the ratio of PMMA:DMF is 0.45:1, the hollow pore size is about 250 nm, and the hollow shell is porous (Fig. S4**b**); when the ratio of PMMA:DMF is 0.5:1, the hollow shell surface appears irregularly with a large hole of 500 nm in length (Fig. S4**c**); when the ratio of PMMA:DMF is 0.55:1, and cracks appear on the hollow shell surface currently (Fig. S4**d**). We chose the best PMMA:DMF ratio of 0.4:1, as shown in Fig. 2**f**, which can keep the pore size at a maximum of 247 nm and still maintain the complete outer carbon

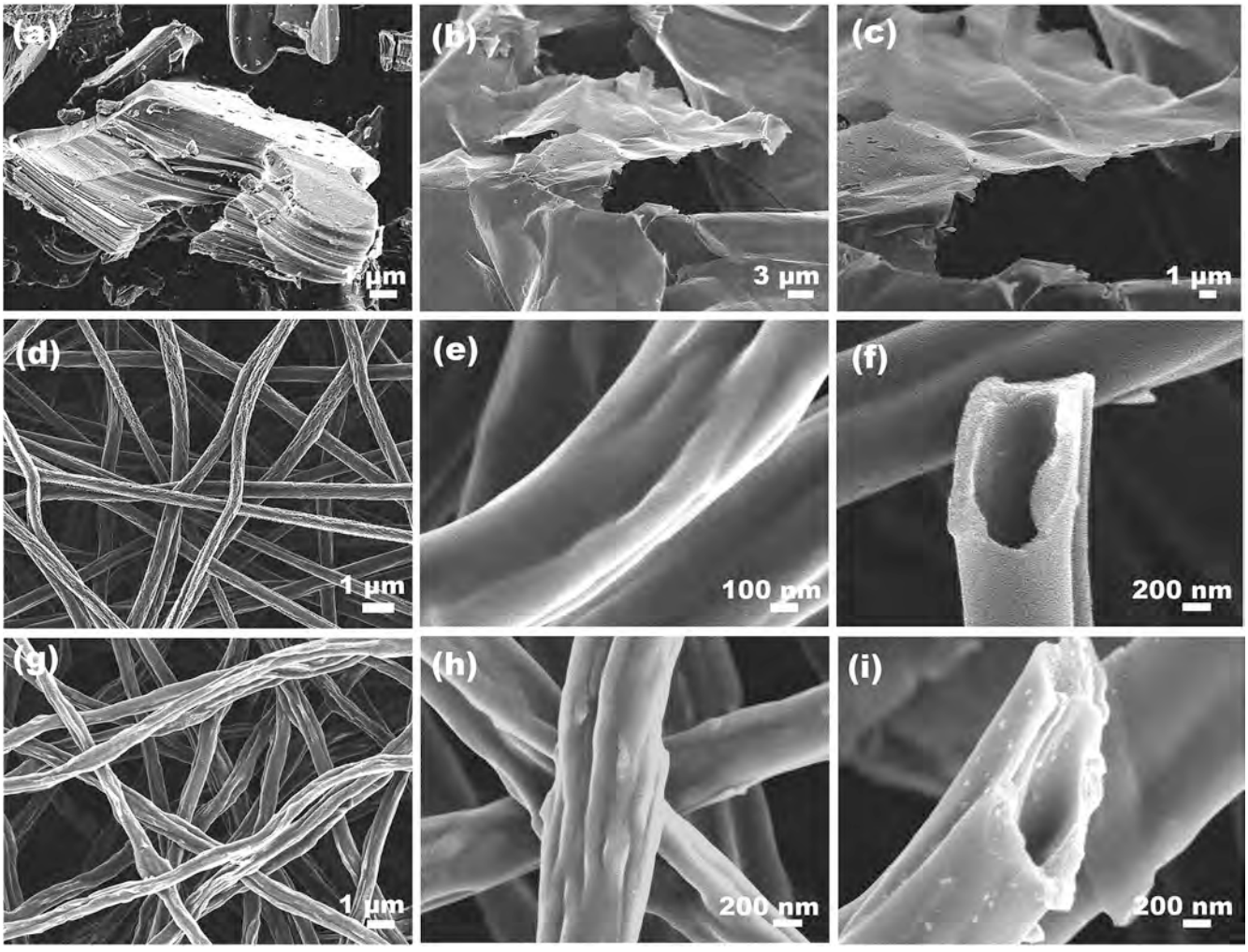

Fig. 2. (a) SEM image of Ti_3AlC_2; (b-c) SEM images of Ti_3C_2 nanosheets; (d) SEM image of Fe_3C/HMCFs; (e) SEM image of MXene/HMCFs; (f) SEM image of HMCFs; (g-i) SEM images of Fe_3C@MXene/HMCFs.

nanofiber structure, providing a complete three-dimensional conductive network for the LIBs during charging and discharging. The experimental results demonstrate that the ratio of PMMA:DMF in the core solution plays a decisive role in the size of the hollow pore size of hollow carbon nanofibers.

By using transmission electron microscopy (TEM), we can further investigate the nanostructure and chemical composition in Fe_3C@MXene/HMCFs composite. As shown in Fig. 3**a**, the distribution of Fe_3C nanoscale particles with an average diameter of 30 nm being dispersed and bent MXene nanosheets can be clearly seen in Fe_3C@MXene/HMCFs with hollow pore sizes up to 247 nm as shown in Fig. 3**b**. At the same time, in order to better study the MXene/HMCFs composites, we investigated the nanostructure and chemical composition of MXene/HMCFs by transmission electron microscopy (**Fig. S2**). The HMCFs appear a hollow multi-channel structure, and the thickness of the shell is about 160 nm which can offer space to relieve the volume changes during the charge and discharge process and provide many active sites. Again, the corresponding SAED plots show the diffraction rings of (2 2 1) and (1 1 0) in Fig. 3**c**. Fig. 3**d** shows the lattice interval with a special separation distance of 0.26 nm, which corresponds to the (1 1 0) crystallographic flat surface of Ti_3C_2. This is powerful evidence of the successful introduction of Ti_3C_2. Fig. 3**f** shows the lattice interval with a spacing of 1.83 nm, which corresponds to the (2 2 1) crystallographic flat surface of Fe_3C and a lattice spacing of 0.337 nm, corresponding to the 002-crystal plane of C, demonstrating the successful introduction of Fe_3C and C once again. Fig. 3**g** shows that the elements (Fe, Ti, C, N and O) in the Fe_3C@MXene/HMCFs composites are uniformly distributed, indicating that MXene and Fe_3C have been successfully added into HMCFs.

XRD, Raman scattering, and XPS are conducted to analyze the structure and composition. Fig. 4**a** shows the X-ray diffraction (XRD) patterns of pure Fe_3C@MXene/HMCFs, Fe_3C/HMCFs and MXene/HMCFs composites. The Fe_3C diffraction peaks in the samples of Fe_3C@MXene/HMCFs materials are consistent with the standard XRD data of Fe_3C (PDF 35–0772), and the diffraction peak at $2\theta = 25.6$ corresponds to the (0 0 2) plane of graphite carbon (PDF 41–1487). As shown in Fig. S1**a**, the prepared $Ti_3C_2T_x$ MXene was subjected to XRD test and exhibited characteristic peaks at 6.8, 13.5, 20, 27, 34.1, 40.7, and 60.9, which verified the successful preparation of $Ti_3C_2T_x$ MXene. Meanwhile, EDS tests were performed on MXene/HMCFs (Fig. S1**b**). The Raman spectra of Fe_3C@MXene/HMCFs, Fe_3C/HMCFs and MXene/HMCFs are shown in Fig. 4**b**. The characteristic peaks located at 216 and 277 cm^{-1} represent Fe_3C, further confirming the presence of Fe_3C [7]. MXene/HMCFs exhibit three peaks belonging to the C-Ti-O vibrations (202.2, 415.7 and 606.7 cm^{-1}) of MXenes and there is no evidence of TiO_2 (150 cm^{-1}). Another two broad peaks at around 1,320 and 1,590 cm^{-1} are assigned to D band from sp_3 type disordered carbon and G band from sp_2 type graphitic carbon [29–31].

The elemental chemical state of the Fe_3C@MXene/HMCFs was characterized by X-ray photoelectron spectroscopy (XPS) technique confirming the existence of Fe, Ti, C, N, O elements within the nanocomposite. As shown in Fig. 4**c**, the Fe 2p spectrum has characteristic peaks at 710.04 eV and 711.12 eV, corresponding to Fe^{3+} $2p_{3/2}$ and Fe^{2+} $2p_{3/2}$, respectively. The characteristic peaks at 724 eV and 726.07 eV correspond to Fe^{2+} $2p_{1/2}$ and Fe^{3+} $2p_{1/2}$, respectively [32–34]. As shown in Fig. 4**d**, the high-resolution Ti 2p XPS spectrum of Fe_3C@MXene/HMCFs can be deconvolved into second doublets corresponding to Ti $2p_{3/2}$ and Ti $2p_{1/2}$. The first doublet at 458.2 and 463.75 eV, the

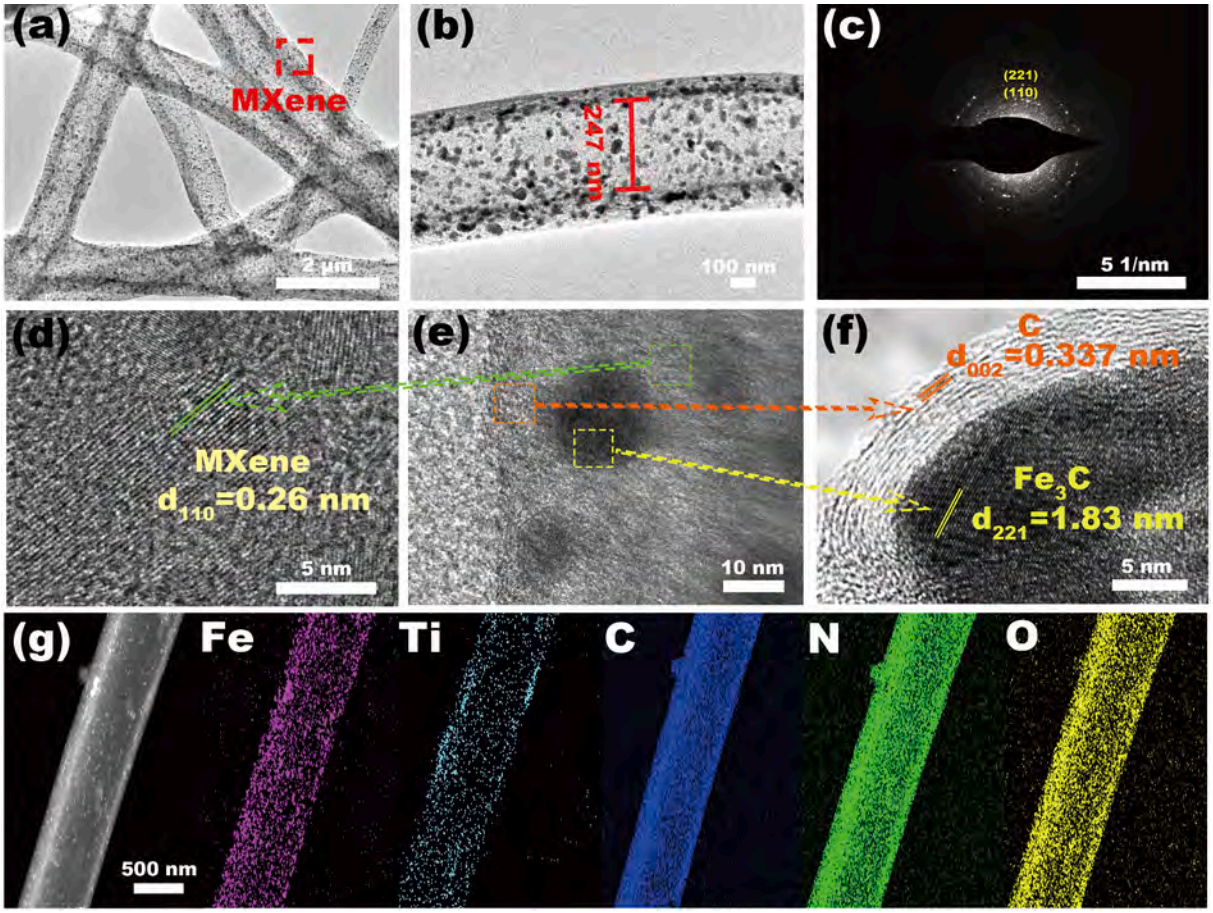

Fig. 3. (a-b) TEM plots of Fe_3C@MXene/HMCFs; (c) SAED pattern of relevant region; (d-f) HRTEM plots of Fe_3C/HMCFs; (g) EDS elemental mappings of Fe_3C@MXene/HMCFs.

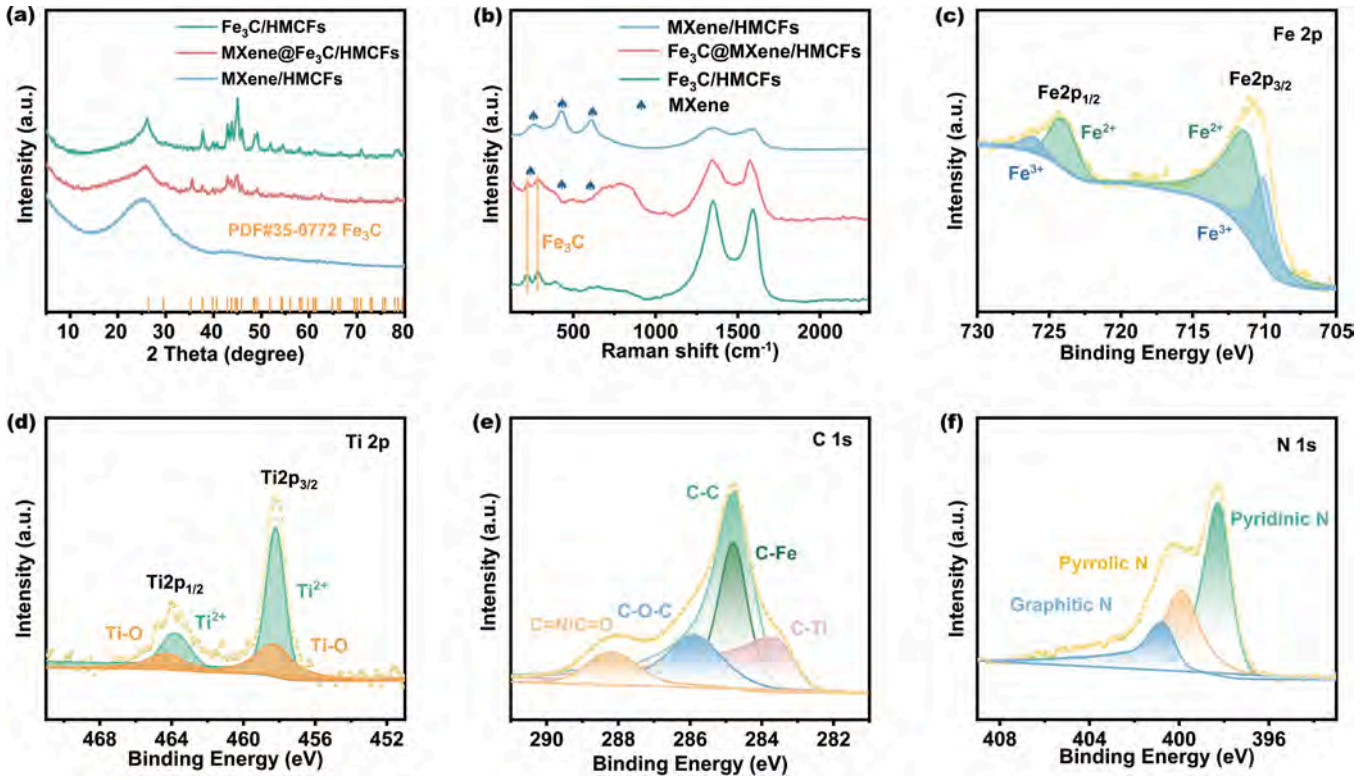

Fig. 4. (a) XRD patterns of Fe_3C@MXene/HMCFs, Fe_3C/HMCFs, MXene/HMCFs and HMCFs; (b) Raman spectra of the Fe_3C@MXene/HMCFs, Fe_3C/HMCFs, MXene/HMCFs and HMCFs; high resolution XPS spectra of (c) Fe 2p, (d) Ti 2p, (e) C 1 s and (f) N 1 s of Fe_3C@MXene/HMCFs.

second doublet at 458.23 and 464.23 eV, and refer to Ti^{2+}, and Ti-O, respectively, which is almost identical to those of pure MXene [35–38]. As illustrated in Fig. 4**e**, the high resolution C 1 s XPS spectrum, reveals the presence of C-Ti (283.6 eV), C-C (284.4 eV), C-Fe (284.77 eV), C-O-C (285.89 eV) and C = N/C = O (288.10 eV) in Fe_3C@MXene/HMCFs [7]. The doping of nitrogen into carbon nanofibers during PAN pyrolysis increases the electron concentration and decreases the Fermi level of carbon nanofibers, thus improving the electrical conductivity. Fig. 4**f** shows three peaks at 398.4 eV, 399.8 eV, and 401.5 eV corresponding to pyridinic-N, pyrrolic-N, and graphitic-N, respectively. The result confirmed that N atoms with different binding bonds were doped into the carbonaceous framework. Moreover, pyridinic and pyrrolic N are lithophilic atoms, which enhance chemisorption and effectively trap Li^+ into the pore channel. Meanwhile, graphitic N improved the charge conductivity of Fe_3C@MXene/HMCFs, which is beneficial for reducing the resistance and promoting the rate performance [39].

To better expound the catalytic mechanism, we measured the CV of Fe_3C@MXene/HMCFs. Fig. 5**a** shows the initial three successive CV curves of the Fe_3C@MXene/HMCFs in the voltage range of 0.01–3 V at a scan rate of 0.1 mV s^{-1}. During the first cathode scan, a weaker reduction peak at about 1.3 V could be found, which can be attributed to the formation of Li_xFe_3C [40]. Besides, the reduction peak at 0.43 V is due to the lithiation process of carbon and the generation of solid electrolyte interface (SEI) films, there is a reduction peak at 1 V which disappeared in the next scans. It corresponds to the insertion of lithium ions and the formation of SEI films. The anodic peak at 1.1 V represents the gradual oxidation of Fe to Li_xFe_3C and Fe^{3+} [41,42]. Starting from the second cycle, the reduction peak moves to 0.8 V. The transformation from Fe to Fe^{3+} or Fe^{2+} resulted in a 0.8 V peak. For the first charge scan course, the 0.2 V peak is regarded as the escape of Li^+ from carbon and the anodic peak located at 1.1 V is designated as the extraction of Li^+ from the SEI film. The transformation from Fe to Fe^{3+} or Fe^{2+} resulted in a 0.8 V change of peak [43–45]. Starting from the second bight, there is no obvious change in the area covered by the cycling curve, which can be proved by the fact that the SEI layer formed in the first cycle and the novel microstructure of the nanocomposites can be efficaciously maintained [46]. The CV curves were also tested for Fe_3C/HMCFs and MXene/HMCFs over a voltage range of 0.01–3 V (Fig. S6). It also illustrates the structural stability of Fe_3C@MXene/HMCFs nanocomposites:

$$Fe_3C + xLi^+ + xe^- \leftrightarrow Li_xFe_3C \quad (1)$$

$$Fe_3C + xLi^+ + xe^- \leftrightarrow 3Fe + Li_xC \quad (2)$$

The electrochemical reaction of Fe_3C with Li^+ includes multiple steps. During the discharging process, Fe_3C reacts with Li^+ to form Li_x-Fe_3C and then Li_xFe_3C is reduced into Fe and Li_XC. During the charging process, Fe reacts with Li_XC while it is oxidized gradually to Fe_3C. The specific reactions are shown in Eq. (1) and the overall reaction is shown in Eq. (2). Fig. 5**b** shows the CV curves of the Fe_3C@MXene/HMCFs electrode at different scanning rates from 0.1 mV s^{-1} to 10 mV s^{-1}. As the scanning rate increases, the peak currents are continuously growing. The first galvanostatic charge/discharge curves of Fe_3C@MXene/HMCFs, Fe_3C/HMCFs, and MXene/ HMCFs at 0.2 A g^{-1} are compared (Fig. 5**c**). The initial discharge capacity (mAh g^{-1}) of Fe_3C@MXene/HMCFs, Fe_3C/HMCFs, and MXene/HMCFs are 1294, 965.7, and 746.3.

Fig. 5**d** shows the EIS analysis of the different electrodes. The different scales of electrode materials of the Nyquist plots all make up a semicircle in the high-frequency region and a sloping line in the low-frequency region. The semicircle in the high-frequency region is counterpart to the migration resistance, which formed the passage of Li^+ through the SEI layer process and the charge transfer resistance at the electrolyte/electrode interface. The diagonal line in the low-frequency region corresponds to the spread process of Li [47–51]. The charge-transfer resistance (R_{ct}) values of Fe_3C@MXene/HMCFs, Fe_3C/HMCFs, and MXene/HMCFs electrodes are 19.1, 50.5, and 59.7 Ω, Fe_3C@MXene/HMCFs exhibit the highest ion conductivity. In the high-frequency region, the semicircular diameter of Fe_3C@MXene/HMCFs is smaller than that of Fe_3C/HMCFs. The synergistic interaction between MXene

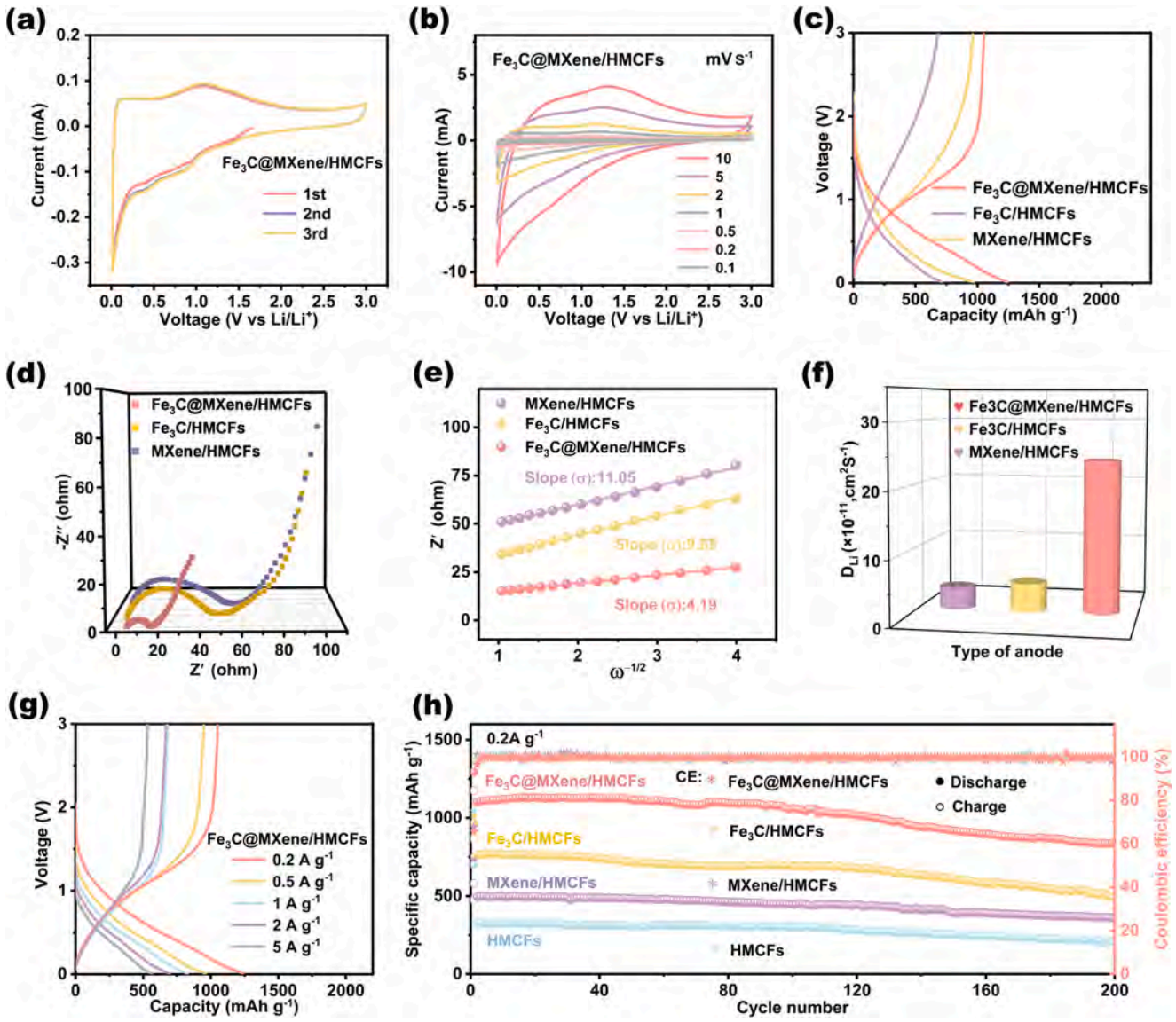

Fig. 5. (a) Cyclic voltammograms of Fe_3C@MXene/HMCFs electrodes at 0.1 mV s^{-1} scan rate; (b) Cyclic voltammograms of Fe_3C@MXene/HMCFs electrodes at different scan rates from 0.1 mV s^{-1} to 10 mV s^{-1}; (c) Comparison of Fe_3C@MXene/HMCFs, Fe_3C/HMCFs and MXene/HMCFs at 0.2 A/g for the first constant-current charge/discharge curves; (d) Nyquist plots of Fe_3C@MXene/HMCFs, Fe_3C/HMCFs and MXene/HMCFs electrodes; (e) Warburg coefficients of Fe_3C@MXene/HMCFs, Fe_3C/HMCFs and MXene/HMCFs electrodes; (f) Li^+ transport coefficients of Fe_3C@MXene/HMCFs, Fe_3C/HMCFs, and MXene/HMCFs electrodes; (g) galvanostatic charge/discharge curves of Fe_3C@MXene/HMCFs at different current densities; (h) Cycling performance of Fe_3C@MXene/HMCFs, Fe_3C/HMCFs and MXene/HMCFs at a high current density of 0.2 A/g.

nanosheets and Fe_3C nanoparticles formed strong conductive channels in hollow carbon nanofibers, which effectively increased the electrical conductivity that is the reason why the semicircular diameter of Fe_3C@MXene/HMCFs in the high-frequency region is smaller than that of Fe_3C/HMCFs and MXene/HMCFs. There is no significant discrepancy in the slope of the low-frequency region, proving an analogous diffusion process of Li^+ in the three types of electrode materials [52,53]. In order to assess Li^+ diffusion at the electrode/electrolyte interface, the diffusion coefficients of lithium ions (D_{Li}) are determined using Eqs. (3)–(5):

$$\omega = 2\pi f \tag{3}$$

$$Z\hat{A} = R_s + R_{ct} + \sigma \times \omega^{-0.5} \tag{4}$$

$$D_{Li} = 0.5R^2T^2/A^2n^4F^4C^2\sigma^2 \tag{5}$$

where R is the gas constant (8.314 J mol^{-1} K^{-1}), σ is the Warburg coefficient, T is the Kelvin temperature (293.15 K), A is the contact area of the electrode (2.01 cm^2), n is the electron number per molecule during the oxidation, F is the Faraday constant (96,485C mol^{-1}) and C is the molar concentration of Li^+ [7,21,54]. The values of σ are derived from the linear relationship between Z′ (the real parts of impedance) and ω (angular frequency), and the corresponding values of D_{Li} are subsequently calculated from Eq. (4). The Warburg coefficients of Fe_3C@MXene/HMCFs, Fe_3C/ HMCFs, and MXene/HMCFs are 4.19, 9.68, and 11.05, as shown in Fig. 5**e**. Fig. 5**f** shows the diffusion coefficients of the lithium ions (D_{Li}) of the Fe_3C@MXene/HMCFs, Fe_3C/HMCFs, and MXene/HMCFs are 2.40×10^{-10}, 4.49×10^{-11}, and 3.44×10^{-11} cm^2 s^{-1}. The results indicate the significant positive effects of Ti_3C_2 MXene on improving electron and ion transport. Fig. 5**g** shows the galvanostatic charge/discharge bights of Fe_3C@MXene/HMCFs at different current densities from 0.2 to 5 A g^{-1}. With the growing of current density, the curves always show better coincidence, which proves that the electrode does not have a great polarization phenomenon [55]. The reason was the introduction of MXene accelerates the ionic reaction kinetics, which

is in accord with the results obtained by electrochemical impedance spectroscopy [56,57]. The Fe_3C@MXene/HMCFs anode has an initial capacity of 1294 mAh g^{-1} at a current density of 0.2 A g^{-1} and maintains a reversible capacity of 831 mAh g^{-1} after 200 turns of charge/discharge cycling (Fig. 5**h**). In comparison, the Fe_3C/HMCFs, MXene/HMCFs and HMCFs anode delivers a lower initial reversible capacity of 965 mAh g^{-1}, 746 mAh g^{-1} and 701 mAh g^{-1} at the same current density. The enhanced Li^+ storage capability for the composite electrode can be attributed to the coherent synergistic effect of Fe_3C and MXene as well as the doping of N atoms [58,59]. Comparison of electrochemical performance on different samples in the reported literature works was shown in **Table S1**, Fe_3C@MXene/HMCFs possessed higher specific capacity. To verify the stability of the negative electrode structure, the battery was disassembled after the cycling performance test, and the morphology and internal structure of the fibers were observed by scanning electron microscopy. As can be seen from Fig. S5, the solid Fe_3C@MXene/HMCFs still maintain the three-dimensional crosslinked network morphology after charge/discharge cycling and there is no obvious fracture, but the carbon nanofibers have shown obvious volume expansion (Fig. S5**a-b**). In contrast, under the same charge/discharge cycling conditions, the hollow Fe_3C@MXene/HMCFs carbon nanofibers showed a clearer 3D crosslinked network morphology without obvious volume expansion, and the internal hollow structure remained intact (Fig. S5**c-d**). It indicates that the carbon nanofibers with hollow structures can provide many active sites during charge–discharge cycling, which effectively alleviates the volume expansion problem. Due to the formation of a stable SEI film on the fiber surface, this SEI film can limit the irreversible depletion of lithium ions induced by each regeneration of the SEI film, which leads to a long-term cycle life. In addition, the three-dimensional interconnection structure of the fibers also remains unchanged, indicating that the electrode structure is not disrupted during repeated intercalation reactions.

To gain insight into the performance of the composites from the electronic and atomic scales, DFT calculations are carried out to explore the electronic structure of the composites and the adsorption energy of the composites for Li^+. Fig. 6**a** shows the crystal structures of Fe_3C/MXene and Fe_3C. The adsorption energies (E_a) of Fe_3C-MXene and Fe_3C composites for lithium ions are −1.71 and −0.93 eV, which indicates that the Fe_3C@MXene/HMCFs composite shows a stronger Li^+ adsorption capability than the Fe_3C/HMCFs, but also has a faster ion/electron transfer rate and more stable structure [60]. We conducted density functional theory (DFT) calculations to obtain the projected density of

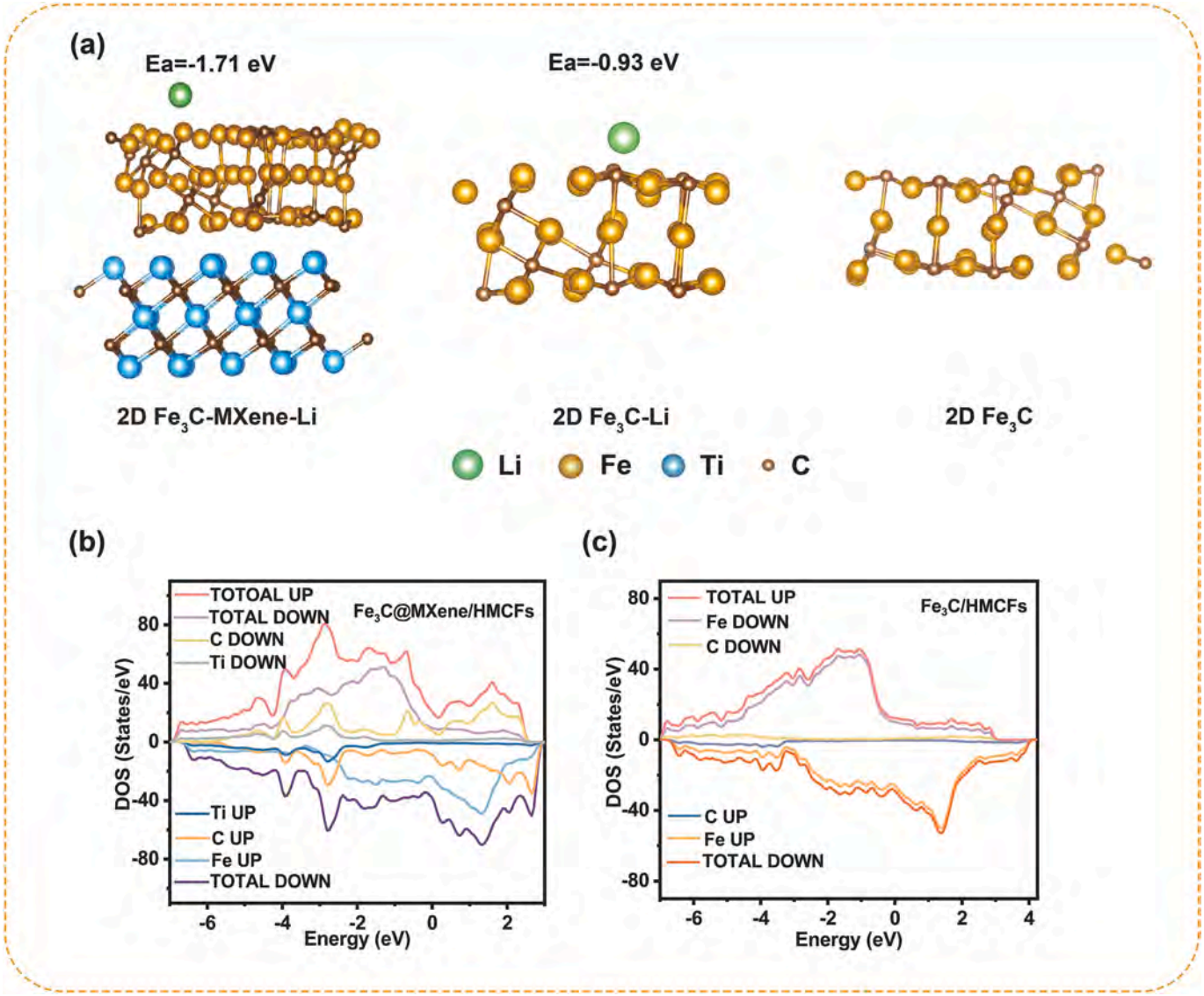

Fig. 6. (a) DFT simulation of the lithium adsorption configuration; (b) Projection density of states for charged samples of Fe_3C@MXene/HMCFs; (c) Projection density of states for charged samples of Fe_3C/HMCFs.

states (DOS) for pristine samples of Fe_3C@MXene/HMCFs and Fe_3C/HMCFs. As shown in Fig. 6**b-c**, the electronic states are continuous near the Fermi energy level, indicating their metallic nature [61]. The DOS of Fe_3C/HMCFs near the Fermi energy level is smaller than that of Fe_3C@MXene/HMCFs, suggesting that their interfacial effects can further enhance the electron/ion conductivity, which is consistent with the test results of EIS [62]. It is also because of the enhanced electronic synergy of Fe_3C@MXene/HMCFs compared to Fe_3C/HMCFs. The enhanced magnetic moment of Fe_3C@MXene/HMCFs compared to Fe_3C/HMCFs indicates that the addition of 2D MXene leads to enhanced interaction between C and Fe, resulting in enhanced binding energy, which is consistent with the above calculations on the adsorption energy of lithium ions.

Based on the electrochemical properties mentioned above, Fe_3C@MXene/HMCFs exhibit the highest discharge specific capacity, optimum rate performance and cycle stability. The excellent electrochemical performance of Fe_3C@MXene/HMCFs anodes can be attributed to the following facts: (i) The hollow carbon nanofiber structure provides a large number of active sites, which effectively mitigates the volume expansion [63]; (ii) The synergistic effect of Fe_3C and MXene forms a strong conductive channel, which effectively enhances the electrical conductivity of Fe_3C@MXene/HMCFs [64]; (iii) DFT calculation shows that MXene coating can effectively enhance the lithium ion adsorption ability of composite electrode materials [10]; (iiii) The N-doped carbon nanofibers derived from PAN provide a second fast electron transport path for the electrode reaction [14].

4. Conclusions

In conclusion, we successfully designed and synthesized a Fe_3C@MXene/HMCFs composite carbon nanofiber with an internal hollow structure by electrostatic spinning and stepwise annealing process. The hollow structure and the synergistic effect of Fe_3C and MXene together construct 3D strong conductive channels, which effectively alleviate the problem of volume expansion, and the double electron channels composed of MXene and N-doped hollow carbon nanofibers [14,65,66], which greatly improve the electrical and ionic conductivity and maintain the structural stability of the composite nanostructure during the lithium battery cycle [67,68]. Fe_3C@MXene/HMCFs film has good electrical conductivity and superior mechanical properties as the negative electrode of LIBs, which enhances the energy density of LIBs battery and shows excellent performance and excellent cycling stability, exhibiting a high initial capacity of 1294 mA h g^{-1} at a current density of 0.2 A g^{-1}, and a capacity of 831 mA h g^{-1} after 200 cycles. The superior electrochemical properties of these flexible composite carbon nanofibers suggest that this unique composite material has promising applications in high-performance lithium-ion batteries.

Declaration of Competing Interest

The authors declare that they have no known competing financial interests or personal relationships that could have appeared to influence the work reported in this paper.

Data availability

Data will be made available on request.

Acknowledgements

This work was financially supported by the National Natural Science Foundation of China (52272219), Natural Science Foundation of Henan Province (222300420255 and 202300410330), City University of Hong Kong Strategic Research Grant (SRG) No. 7005505, and City University of Hong Kong Donation Research Grants (DON-RMG 9229021 and 9220061).

Appendix A. Supplementary data

Supplementary data to this article can be found online at https://doi.org/10.1016/j.cej.2023.147366.

References

[1] W. Yan, Z. Mu, Z. Wang, Y. Huang, D. Wu, P. Lu, J. Lu, J. Xu, Y. Wu, T. Ma, M. Yang, X. Zhu, Y. Xia, S. Shi, L. Chen, H. Li, F. Wu, Hard-carbon-stabilized Li-Si anodes for high-performance all-solid-state Li-ion batteries, Nat. Energy 8 (2023) 800–813.
[2] Z. Li, I. Sami, J. Yang, J. Li, R.V. Kumar, M. Chhowalla, Lithiated metallic molybdenum disulfide nanosheets for high-performance lithium-sulfur batteries, Nat. Energy 8 (2023) 84–93.
[3] H. Li, S. Ma, H. Cai, H. Zhou, Z. Huang, Z. Hou, J. Wu, W. Yang, H. Yi, C. Fu, Y. Kuang, Ultra-thin Fe_3C nanosheets promote the adsorption and conversion of polysulfides in lithium-sulfur batteries, Energy Storage Mater. 18 (2019) 338–348.
[4] L. Wang, Y. Zhang, P.G. Bruce, Batteries for wearables, Natl. Sci. Rev. 10 (2023) nwac062.
[5] K. Xu, Manipulating interphases in batteries, Natl. Sci. Rev. 4 (2017) 19–20.
[6] D. Wu, R. Shen, R. Yang, W. Ji, M. Jiang, W. Ding, L. Peng, Mixed Molybdenum Oxides with Superior Performances as an Advanced Anode Material for Lithium-Ion Batteries, Sci. Rep. 7 (2017) 44697.
[7] Y. Guo, D. Zhang, Y. Yang, Y. Wang, Z. Bai, P.K. Chu, Y. Luo, MXene-encapsulated hollow Fe_3O_4 nanochains embedded in N-doped carbon nanofibers with dual electronic pathways as flexible anodes for high-performance Li-ion batteries, Nanoscale 13 (2021) 4624–4633.
[8] F. Wu, J. Maier, Y. Yu, Guidelines and trends for next-generation rechargeable lithium and lithium-ion batteries, Chem. Soc. Rev. 49 (2020) 1569–1614.
[9] C. Zheng, Y. Yao, X. Rui, Y. Feng, D. Yang, H. Pan, Y. Yu, Functional MXene-Based Materials for Next-Generation Rechargeable Batteries, Adv. Mater. 34 (2022) 2204988.
[10] H. Zhou, J. Zhang, J. Liu, S. Feng, C. Li, E. Marsili, X. Zhang, Silicon Nanospheres Supported on Conductive MXene Nanosheets as Anodes for Lithium-Ion Batteries, ACS Appl. Energy Mater. 6 (2022) 160–169.
[11] P. Huang, W.Q. Han, Recent Advances and Perspectives of Lewis Acidic Etching Route: An Emerging Preparation Strategy for MXenes, Nano-Micro Lett. 15 (2023) 68.
[12] T. Koriukina, A. Kotronia, J. Halim, M. Hahlin, J. Rosen, K. Edstrom, L. Nyholm, On the Use of $Ti_3C_2T_x$ MXene as a Negative Electrode Material for Lithium-Ion Batteries, ACS Omega 7 (2022) 41696–41710.
[13] L. Yang, J. Wang, A. Li, H. Liu, M. Zhang, Z. Shen, Low-temperature carbonization of p-Phenylenediamine guided by an iron alginate template for lithium-ion capacitors, New J. Chem. 46 (2022) 12229–12236.
[14] X. Cao, C. Ma, L. Luo, L. Chen, H. Cheng, R.S. Orenstein, X. Zhang, Nanofiber Materials for Lithium-Ion Batteries, Adv. Fiber Mater. 5 (2023) 1141–1197.
[15] D. Sun, M. Wang, Z. Li, G. Fan, L.-Z. Fan, A. Zhou, Two-dimensional Ti_3C_2 as anode material for Li-ion batteries, Electrochem. Commun. 47 (2014) 80–83.
[16] D. Seo, M.R. Kim, J. Kyu Song, E. Kim, J. Koo, K.C. Kim, H. Han, Y. Lee, C. Won Ahn, Hollow Ti3C2 MXene/Carbon Nanofibers as an Advanced Anode Material for Lithium-Ion Batteries, ChemElectroChem 9 (2022) e202101344.
[17] D. Qiu, B. Zhang, T. Zhang, T. Shen, Z. Fang, W. Zhao, J. Xu, Y. Hou, Flexible Co_9S_8-Carbon Nanofibers Architecture for Lithium-Ion Batteries: A Comprehensive Study of the Nature of Lithium Storage, ACS Mater. Lett. 5 (2023) 1488–1496.
[18] W. Lei, X. Wang, Y. Zhang, Z. Luo, P. Xia, Y. Zou, Z. Ma, Y. Pan, S. Lin, Facile synthesis of Fe_3C nano-particles/porous biochar cathode materials for lithium sulfur battery, J. Alloys Compd. 853 (2021), 157024.
[19] M. Zhang, J. Mu, Y. Li, Y. Pan, Z. Dong, B. Chen, S. Guo, W. Yuan, H. Fang, H. Hu, M. Wu, Propelling polysulfide redox by Fe_3C-FeN heterostructure@nitrogen-doped carbon framework towards high-efficiency Li-S batteries, J. Energy Chem. 78 (2023) 105–114.
[20] Z. Jin, M. Zhao, T. Lin, Z. Wang, Q. Zhang, B. Liu, L. Li, L. Chen, L. Zhang, Z. Su, C. Wang, Ordered micro-mesoporous carbon spheres embedded with well-dispersed ultrafine Fe_3C nanocrystals as cathode material for high-performance lithium-sulfur batteries, Chem. Eng. J. 388 (2020), 124315.
[21] L. Su, Y. Zhong, Z. Zhou, Role of transition metal nanoparticles in the extra lithium storage capacity of transition metal oxides: a case study of hierarchical core-shell Fe_3O_4@C and Fe@C microspheres, J. Mater. Chem. A 1 (2013) 15158–15166.
[22] Y. Zhong, M. Yang, X. Zhou, Y. Luo, J. Wei, Z. Zhou, Orderly packed anodes for high-power lithium-ion batteries with super-long cycle life: rational design of $MnCO_3$/large-area graphene composites, Adv. Mater. 27 (2015) 806–812.
[23] Y. Guo, D. Zhang, Z. Bai, Y. Yang, Y. Wang, J. Cheng, P.K. Chu, Y. Luo, MXene nanofibers confining MnO_x nanoparticles: a flexible anode for high-speed lithium ion storage networks, Dalton Trans. 51 (2022) 1423–1433.
[24] S. Shi, Z. Li, L. Shen, X. Yin, Y. Liu, G. Chang, J. Wang, S. Xu, J. Zhang, Y. Zhao, Electrospun free-standing FeP@NPC film for flexible sodium ion batteries with remarkable cycling stability, Energy Storage Mater. 29 (2020) 78–83.
[25] F. Liang, H. Dong, Z. Ji, W. Zhang, H. Zhang, C. Cao, H. Li, H. Liu, K.-Q. Zhang, Y. Lai, Y. Tang, M. Ge, Temperature-dependent synthesis of SnO_2 or Sn embedded in hollow porous carbon nanofibers toward customized lithium-ion batteries, Sci. China Mater. 66 (2023) 1736–1746.
[26] X. Li, B. Cheng, G. Guan, X. Zhang, K. Zhang, J. Xiang, Flexible electrospun FeCo/carbon hybrid nanofiber films as binder-free anodes for enhanced lithium storage performance, Electrochim. Acta 454 (2023), 142420.

[27] L. Xie, J. Bi, X. Gao, L. Meng, C. Liu, J. Rong, Preparation of hollow core-shell structured Ti_3C_2@Ti_2SnC/CNFs with stable electrochemical performance as anode material for lithium ion battery, Ceram. Int. 49 (2023) 23003–23010.

[28] P. Ding, T. Yan, K. Li, Q. Wu, X. Zhu, H. Chen, A. Ju, Freestanding TiO@ heteroatom-doped hollow multi-channel carbon fibers for lithium-sulfur batteries, J. Alloys Compd. 928 (2022), 167056.

[29] A.S. Levitt, M. Alhabeb, C.B. Hatter, A. Sarycheva, G. Dion, Y. Gogotsi, Electrospun MXene/carbon nanofibers as supercapacitor electrodes, J. Mater. Chem. A 7 (2019) 269–277.

[30] C. Wei, H. Liu, R. Gan, W. Ma, Y. Wang, Y. Han, Y. Song, C. Ma, J. Shi, Flexible $NiCo_2S_4$-hollow carbon nanofibers electrocatalytic membrane as an advanced interlayer for lithium-sulfur batteries, Colloid. Surf. A 648 (2022), 129179.

[31] L. Chen, Z. Li, G. Li, M. Zhou, B. He, J. Ouyang, W. Xu, W. Wang, Z. Hou, A facile self-catalyzed CVD method to synthesize Fe_3C/N-doped carbon nanofibers as lithium storage anode with improved rate capability and cyclability, J. Mater. Sci. Technol. 44 (2020) 229–236.

[32] Z. Xiong, J. Li, Y. Sun, Y. Lin, L. Du, Z. Wei, M. Wu, K. Shi, Q. Liu, Fe_3C@NCNT as a promoter for the sulfur cathode toward high-performance lithium-sulfur batteries, J. Alloys Compd. 899 (2022), 163245.

[33] J. Lu, J. Liu, X. Gong, Z. Wang, Fe_3C doped modified nano-Si/C composites as high-coulombic-efficiency anodes for lithium-ion batteries, Sustain. Energ. Fuels 5 (2021) 6170–6180.

[34] Q.D. Ruan, R. Feng, J.J. Feng, Y.J. Gao, L. Zhang, A.J. Wang, High-Activity Fe_3C as pH-Universal Electrocatalyst for Boosting Oxygen Reduction Reaction and Zinc-Air Battery, Small 2300136 (2023).

[35] W. Eom, H. Shin, R.B. Ambade, S.H. Lee, K.H. Lee, D.J. Kang, T.H. Han, Large-scale wet-spinning of highly electroconductive MXene fibers, Nat. Commun. 11 (2020) 2825.

[36] S.-X. Yan, S.-H. Luo, Q. Wang, Y.-H. Zhang, X. Liu, Rational design of hierarchically sulfide and MXene-reinforced porous carbon nanofibers as advanced electrode for high energy density flexible supercapacitors, Compos. Part B-Eng. 224 (2021), 109246.

[37] Y. Ma, H. Sheng, W. Dou, Q. Su, J. Zhou, E. Xie, W. Lan, Fe_2O_3 Nanoparticles Anchored on the $Ti_3C_2T_x$ MXene Paper for Flexible Supercapacitors with Ultrahigh Volumetric Capacitance, ACS Appl. Mater. Interfaces 12 (2020) 41410–41418.

[38] L. Hong, S. Ju, Y. Yang, J. Zheng, G. Xia, Z. Huang, X. Liu, X. Yu, Hollow-shell structured porous $CoSe_2$ microspheres encapsulated by MXene nanosheets for advanced lithium storage, Sustain. Energ. Fuels 4 (2020) 2352–2362.

[39] M. Ye, F. Hu, D. Yu, S. Han, L. Li, S. Peng, Hierarchical FeC/MnO_2 composite with in-situ grown CNTs as an advanced trifunctional catalyst for water splitting and Metal-Air batteries, Ceram. Int. 47 (2021) 18424–18432.

[40] T. Xiang, Z. Chen, Z. Rao, M. Yan, Z. Feng, X. Li, H. Yang, J. Huang, X. Shen, Hierarchical Fe/Fe_3C/C nanofibers as anodes for high capacity and rate in lithium ion batteries, Ionics 27 (2021) 3663–3669.

[41] A. Gangwar, A. Sharma, S.K. Shaw, S. Singh Meena, N.K. Prasad, Structural and electrochemical performance studies for nanocomposites of carbon with Fe3C or Mn-Substituted (Fe3C/Fe3O4) as anodes for Li-batteries, Appl. Surf. Sci. 533 (2020), 147474.

[42] X. Liu, X. Li, Y. Sun, S. Zhang, Y. Wu, Onion-like carbon coated Fe_3C nanocapsules embedded in porous carbon for the stable lithium-ion battery anode, Appl. Surf. Sci. 479 (2019) 318–325.

[43] S. Li, J. Qin, T. Gao, J. Du, K. Yuan, N. Li, L. Xu, J. Xu, Fabrication of Fe_3C nanoparticles embedded in N-doped carbon nanotubes/porous carbon 3D materials derived from distilled grains for high performance of potassium ion battery, J. Alloys Compd. 912 (2022), 165130.

[44] M. Zou, L. Wang, J. Li, L. Guan, Z. Huang, Enhanced Li-ion battery performances of yolk-shell Fe_3O_4@C anodes with Fe_3C catalyst, Electrochim. Acta 233 (2017) 85–91.

[45] C. Zhao, R. Fan, B. Murugesan, Y. Xu, J. Ma, J. Yao, I. Krucinska, Y. Cai, J. Gao, Uniformly inserted Fe_3C nanoparticles in sericin-derived hierarchical porous carbon for high-performance Li-ion battery, J. Alloys Compd. 881 (2021), 160661.

[46] W. Shen, W. Kou, Y. Liu, Y. Dai, W. Zheng, G. He, S. Wang, Y. Zhang, X. Wu, S. Fan, X. Li, Fe_3C-doped asymmetric porous carbon membrane binder-free integrated materials as high performance anodes of lithium-ion batteries, Chem. Eng. J. 368 (2019) 310–320.

[47] M. Cao, W. Wu, R. Guo, Y. Liang, G. Pan, H. Wu, X. Liu, J. Zhang, Molten salt synthesis of NiCo-$NiCo_2O_4$@C nanotubes as anode materials for Li-ion batteries, J. Colloid Interf. Sci. 636 (2023) 518–527.

[48] I. Pathak, D. Acharya, K. Chhetri, P. Chandra Lohani, T. Hoon Ko, A. Muthurasu, S. Subedi, T. Kim, S. Saidin, B. Dahal, H., Yong Kim, $Ti_3C_2T_x$ MXene integrated hollow carbon nanofibers with polypyrrole layers for MOF-derived freestanding electrodes of flexible asymmetric supercapacitors, Chem. Eng. J. 469 (2023), 143388.

[49] R. Zhang, J. Dong, W. Zhang, L. Ma, Z. Jiang, J. Wang, Y. Huang, Synergistically coupling of 3D FeNi-LDH arrays with $Ti_3C_2T_x$-MXene nanosheets toward superior symmetric supercapacitor, Nano Energy 91 (2022), 106633.

[50] B. Liu, K. Jiang, K. Zhu, X. Liu, K. Ye, J. Yan, G. Wang, D. Cao, Cable-like polyimide@carbon nanotubes composite as a capable anode for lithium ion batteries, Chem. Eng. J. 446 (2022), 137208.

[51] D. Liu, Z. Wang, Z. Guo, Y. Tian, C. Wang, Electrospun CuCoN(0.6) coating necklace-like N-doped carbon nanofibers for high performance lithium-sulfur batteries, J. Colloid Interf. Sci. 645 (2023) 705–714.

[52] Y. Xiao, T. Li, Y. Mao, X. Hao, W. Wang, S. Meng, J. Wu, J. Zhao, Core-shell N-doped carbon embedded Co_3O_4 nanoparticles with interconnected and hierarchical porous structure as superior anode materials for lithium-ion batteries, J. Energy Storage 63 (2023), 106998.

[53] M. Qi, M. Hu, J. Xu, X. Yuan, Z. Zhang, Smart construction of $Ti_2Nb_{10}O_{29}$/carbon nanofiber core-shell composite arrays as anode materials for lithium-ion batteries, J. Alloys Compd. 886 (2021), 161146.

[54] X. Liu, H. Liu, Y. Cao, X. Wu, Z. Shan, Silicon Nanoparticles Embedded in Chemical-Expanded Graphite through Electrostatic Attraction for High-Performance Lithium-Ion Batteries, ACS Appl. Mater. Interfaces 15 (2023) 9457–9464.

[55] F. Ming, H. Liang, G. Huang, Z. Bayhan, H.N. Alshareef, MXenes for Rechargeable Batteries Beyond the Lithium-Ion, Adv. Mater. 33 (2021) 2004039.

[56] Y. Huang, Q. Lu, D. Wu, Y. Jiang, Z. Liu, B. Chen, M. Zhu, O.G. Schmidt, Flexible MXene films for batteries and beyond, Carbon Energy 4 (2022) 598–620.

[57] J.-M. Yoon, Y.-H. Lee, C.-M. Park, Optimized Ga-based nanocomposite for superior Li-ion battery anodes, Mater. Today Energy 35 (2023), 101327.

[58] W. Ding, S. Wang, X. Wu, Y. Wang, Y. Li, P. Zhou, T. Zhou, J. Zhou, S. Zhuo, $Co_{0.85}Se$@C/$Ti_3C_2T_x$ MXene hybrids as anode materials for lithium-ion batteries, J. Alloys Compd. 816 (2020), 152566.

[59] W. Wang, D. Jiang, X. Chen, K. Xie, Y. Jiang, Y. Wang, A sandwich-like nano-micro LDH-MXene-LDH for high-performance supercapacitors, Appl. Surf. Sci. 515 (2020), 145982.

[60] M. Wang, P.F. Fang, Y. Chen, X.Y. Leng, Y. Yan, S.B. Yang, P. Xu, C. Yan, Synthesis of Highly Stable LTO/rGO/SnO2 Nanocomposite via In Situ Electrostatic Self-Assembly for High-performance Lithium-Ion Batteries, Adv. Funct. Mater. 33 (2023) 2213902.

[61] Z. Bai, D. Zhang, Y. Guo, Y. Yang, H. Yan, Y. Wang, J. Cheng, P.K. Chu, H. Pang, Y. Luo, Hierarchical Cobalt-Nickel Double Hydroxide Arrays Assembled on Naturally Sedimented Ti3C2Tx for High-Performance Flexible Supercapacitors, Adv. Sustain. Syst. 6 (2022) 2100371.

[62] Y. Niu, Z. Hu, B. Zhang, D. Xiao, H. Mao, L. Zhou, F. Ding, Y. Liu, Y. Yang, J. Xu, W. Yin, N. Zhang, Z. Li, X. Yu, H. Hu, Y. Lu, X. Rong, J. Li, Y.S. Hu, Earth-Abundant Na-Mg-Fe-Mn-O Cathode with Reversible Hybrid Anionic and Cationic Redox, Adv. Energy Mater. 13 (2023) 2300746.

[63] Y. Zhao, J. Yan, J. Yu, B. Ding, Electrospun Nanofiber Electrodes for Lithium-Ion Batteries, Macromol. Rapid Comm. 44 (2023) 2200740.

[64] E. Lee, T.U. Wi, J. Park, S.W. Park, M.H. Kim, D.H. Lee, B.C. Park, C. Jo, R. Malik, J. H. Lee, T.J. Shin, S.J. Kang, H.W. Lee, J. Lee, D.H. Seo, Nanocomposite Engineering of a High-Capacity Partially Ordered Cathode for Li-Ion Batteries, Adv. Mater. 35 (2023) 2208423.

[65] X. Ni, Z. Cui, N. Jiang, H. Chen, Q. Wu, A. Ju, M. Zhu, Hollow multi-nanochannel carbon nanofiber/MoS_2 nanoflower composites as binder-free lithium-ion battery anodes with high capacity and ultralong-cycle life at large current density, J. Mater. Sci. Technol. 77 (2021) 169–177.

[66] J. Chen, X.-L. Chen, R. Lu, Y. Li, A.-Q. Pan, Necklace-like carbon nanofibers encapsulating MoO_2 nanospheres with Mo-C bonding for stable lithium-ion storage, Rare Metals 42 (2023) 2592–2600.

[67] X. He, X. Wang, M. Tang, H. Zhang, Y. Wang, Self-supporting ZnP_2@N, P co-doped carbon nanofibers as high-performance anode material for lithium-ion batteries, J. Alloys Compd. 897 (2022), 163235.

[68] S. Hong, J. Nam, S. Park, D. Lee, M. Park, D.S. Lee, N.D. Kim, D.-Y. Kim, B.-C. Ku, Y.A. Kim, J.Y. Hwang, Carbon nanotube fibers with high specific electrical conductivity: Synergistic effect of heteroatom doping and densification, Carbon 184 (2021) 207–213.

Supporting Information

Highly flexible multilayer MXene hollow carbon nanofibers confined with Fe_3C particles for high-performance lithium-ion batteries

Xiaohong Lu [1], Jinbing Cheng [1,*], Dawei Zhou [1], Yichong Chen [1], Hao Jiang [1], Yang Lu [2], Deyang Zhang [2], Dezhi Kong [5], Paul K. Chu [4], Hui Ying Yang [3,*], and Yongsong Luo [1,2,*]

[1] Henan International Joint Laboratory of MXene Materials Microstructure, College of Physics and Electronic Engineering, Nanyang Normal University, Nanyang 473061, P. R. China

[2] Key Laboratory of Microelectronics and Energy of Henan Province, Engineering Research Center for MXene Energy Storage Materials of Henan Province, Henan Joint International Research Laboratory of New Energy Storage Technology, Xinyang Normal University, Xinyang 464000, P. R. China

[3] Pillar of Engineering Product Development, Singapore University of Technology and Design, 8 Somapah Road, 487372 Singapore, Singapore

[4] Department of Physics, Department of Materials Science & Engineering, and Department of Biomedical Engineering, City University of Hong Kong, Tat Chee Avenue, Kowloon, Hong Kong, China

[5] Key Laboratory of Material Physics, Ministry of Education, School of Physics and Microelectronics, Zhengzhou University, Zhengzhou 450052, P. R. China

[*] Corresponding authors: chengjinbing1988@163.com (J.B. Cheng); yanghuiying@sutd.edu.sg (H. Y. Yang); ysluo@xynu.edu.cn (Y.S. Luo)

1. Materials

Polyacrylonitrile (PAN, Mw=250,000) was purchased from macklin; polymethyl methacrylate was purchased from China Plastics; Ti_3AlC_2 (99.9%) was purchased from Sunene Technology; anhydrous ferric chloride ($FeCl_3$, 99.9%) was purchased from aladin; N, N-dimethylformamide (DMF, 99.5%) was purchased from aladin. All reagents were analytical grade reagents, and no further purification was required for use.

2. Preparation of $Ti_3C_2T_x$ MXene

1 g of lithium fluoride was added to 30 ml, 9 mol/L hydrochloric acid at a temperature below 40 °C. After stirring for 5 min, 5 ml of 40% hydrofluoric acid was added and stirred for 15 min. After that, Ti_3AlC_2 was added in several times within one and a half hours. The mixture was kept below 40 °C and stirred for 12 hours to allow the hydrofluoric acid to etch Al accurately from Ti_3AlC_2. The solution was centrifuged at 5000 rpm until it became a suspension, after pH≧6. The $Ti_3C_2T_x$ MXene solution was transferred to the bottle and sonicated in low temperature for one hour and then sonicated by argon gas for one hour. For the product to be applied in the electrostatic spinning of this experiment, the product was centrifuged with dimethylformamide (DMF) at 10,000 rpm for 1.2 h at 30 °C. Repeating this operation twice, a solution of $Ti_3C_2T_x$ MXene will be obtained.

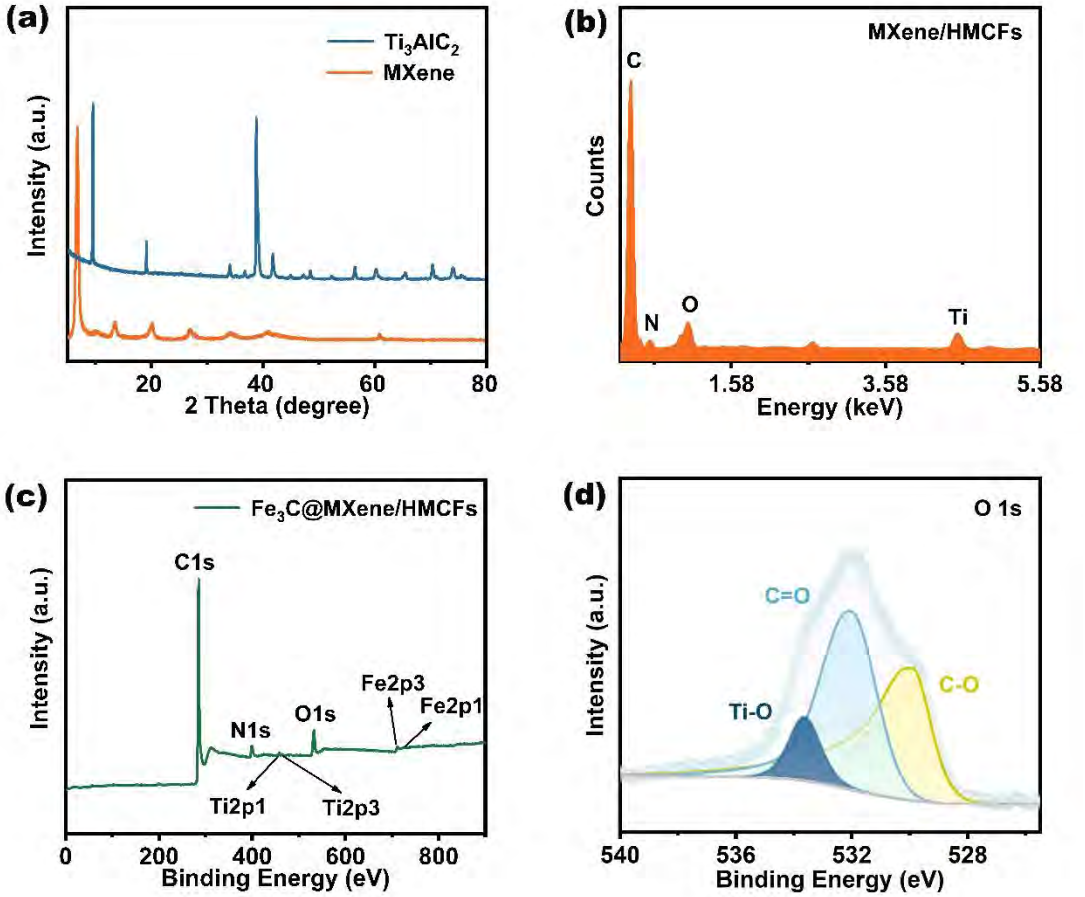

Fig. S1. (a) XRD patterns of MXene and Ti_3AlC_2; (b) EDS elemental of HMCFs; (c) XPS survey spectra of Fe_3C@MXene/HMCFs; (d) High-resolution XPS spectra of O1s.

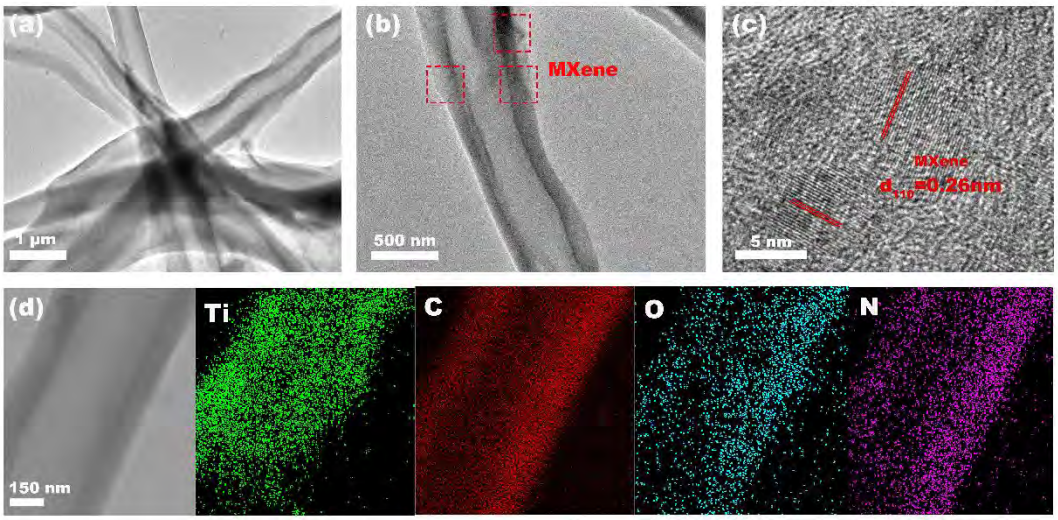

Fig. S2. (a-b) TEM plots of MXene/HMCFs; (c) HRTEM plot of Exploration of MXene/HMCFs; (d) EDS elemental mappings of MXene/HMCFs.

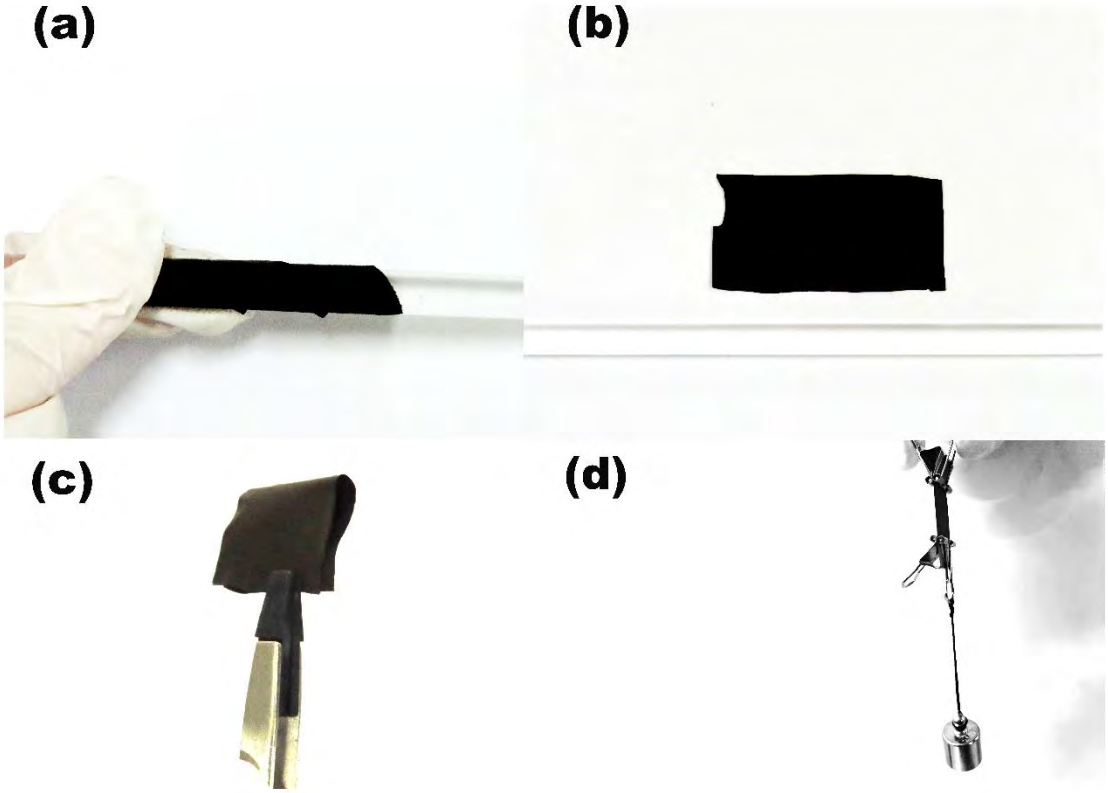

Fig. S3. (a-d) Digital photographs of the flexible Fe_3C@MXene/HMCFs films.

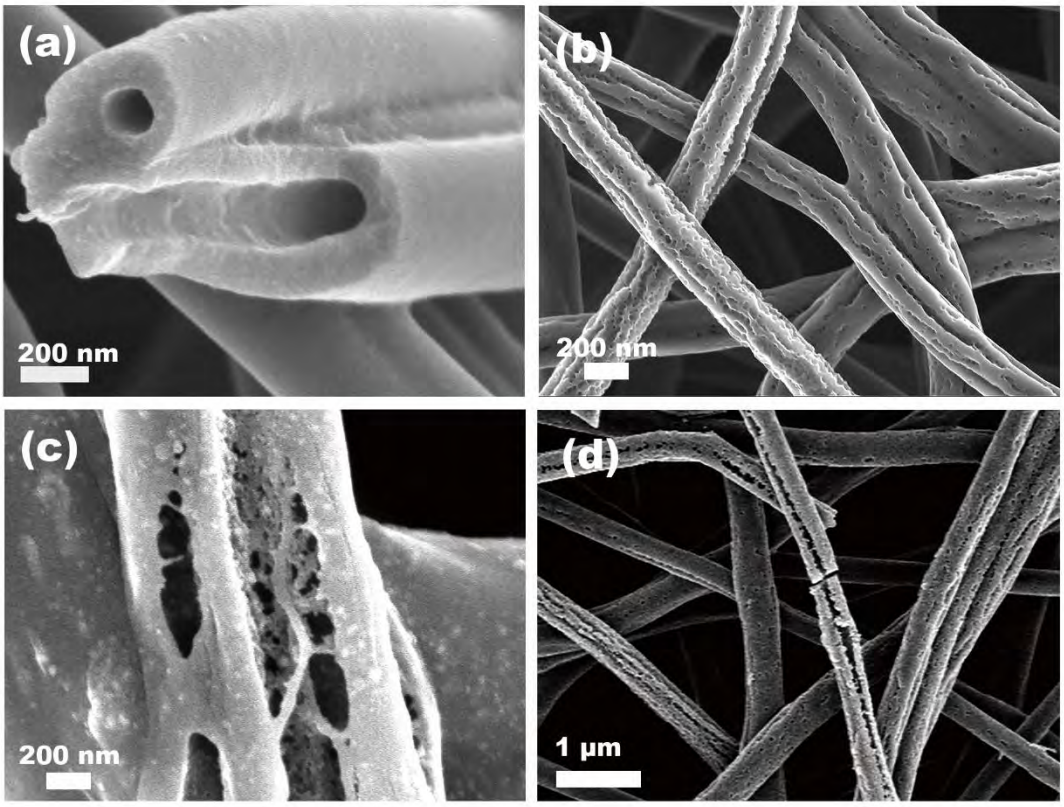

Fig. S4. (a-d) SEM images of HMCFs with PMMA:DMF ratios of 0.3, 0.45, 0.5, 0.55:1, respectivel.

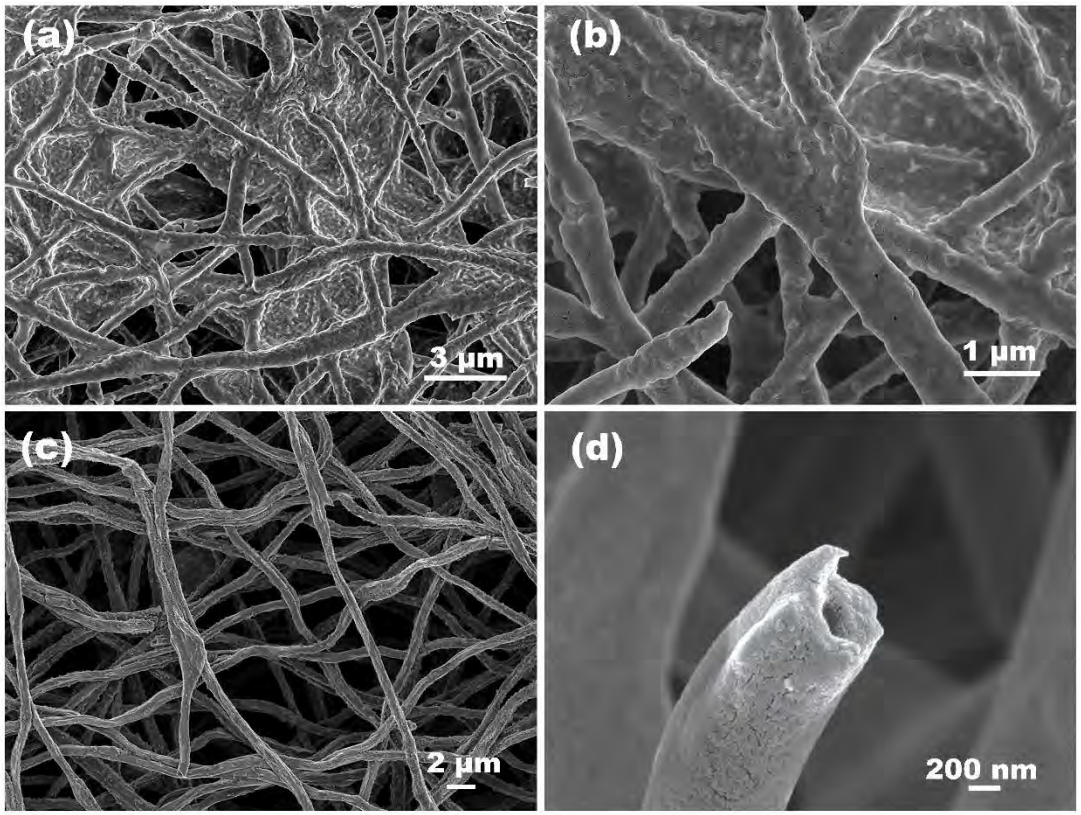

Fig. S5. (a-b) SEM images of solid Fe_3C@MXene/HMCFs after cycling; (c-d) SEM images of internal hollow Fe_3C@MXene/HMCFs after cycling.

Table S1 Comparison of electrochemical performance on different samples in the reported literature works

Anode materials	Current density ($A\ g^{-1}$)	Cycle number	Specific Capacity ($mAh\ g^{-1}$)	Reference
Fe_3C@MXene/HMCFs	0.2	200	1100	This work
Fe_3C@CNCs/EG	0.06	75	1226.2	1
CSGC@Fe_3C	0.1	100	423	2
Graphitic carbon encapsulated	5	200	302	3
Fe_3C/APCM	0.1	200	605	4
Fe_3C@N-CNPC	0.1	570	256	5
Si@Fe_3C/N-C	0.5	200	1300	6
Fe/Fe_3C/C nanofibers	1	1200	663	7
C/Fe_3C composite	0.1	120	750	8
Fe_3C/SC	0.1	150	584	9
Ti_3C_2	2.6	100	126	10
Co_9S_8@MXene/CNFs	1	750	406	11
Ti_3C_2 MXene/Carbon Nanofibers	0.4	100	334	12
MnO_x-MXene/CNFs	2	2000	1098	13
Fe_3O_4@MXene/CNFs	2	500	800	14
Ti_3C_2@Ti_2SnC/CNFs	0.4	300	320	15

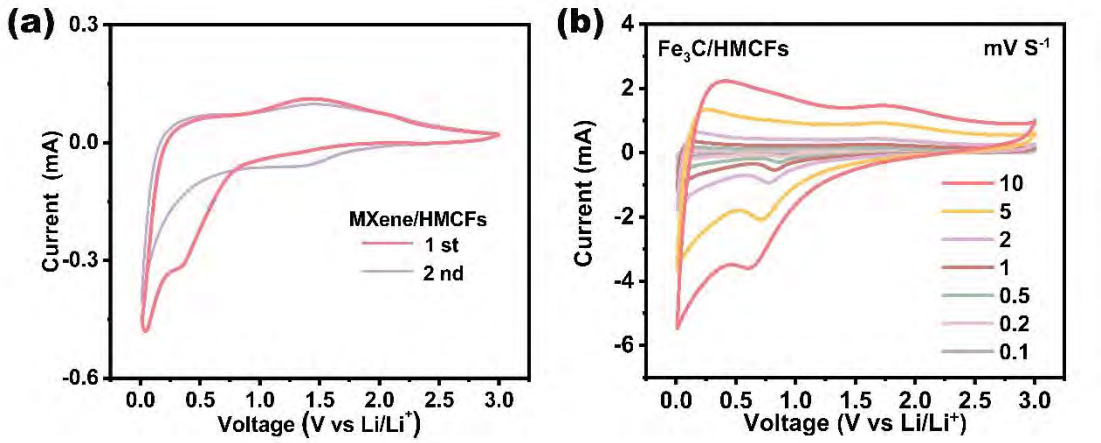

Fig. S6. (a) Cyclic voltammograms of MXene/HMCFs electrodes at 0.1 mV s^{-1} scan rate; (b) Cyclic voltammograms of Fe_3C /HMCFs electrodes at different scan rates from 0.1 mV s^{-1} to 10mV s^{-1}.

References

[1] Y.-G. Huang, X.-L. Lin, X.-H. Zhang, Q.-C. Pan, Z.-X. Yan, H.-Q. Wang, J.-J. Chen, Q.-Y. Li, Fe_3C@carbon nanocapsules/expanded graphite as anode materials for lithium ion batteries, Electrochim. Acta 178 (2015) 468-475.

[2] B. Li, Y. Zhang, J. Xiong, Y. Gui, T. Huang, J. Peng, H. Liu, F. Yang, M. Li, Chitosan-derived graphitic carbon@Fe_3C as anode materials for lithium ion battery, J. Mater. Sci. 57 (2022) 9939-9954.

[3] Y. Liu, X. Li, A.K. Haridas, Y. Sun, J. Heo, J.-H. Ahn, Y. Lee, Biomass-Derived Graphitic Carbon Encapsulated Fe/Fe_3C Composite as an Anode Material for High-Performance Lithium-Ion Batteries, Energies 13 (2020) 827.

[4] W. Shen, W. Kou, Y. Liu, Y. Dai, W. Zheng, G. He, S. Wang, Y. Zhang, X. Wu, S. Fan, X. Li, Fe_3C-doped asymmetric porous carbon membrane binder-free integrated materials as high-performance anodes of lithium-ion batteries, Chem. Eng. J. 368 (2019) 310-320.

[5] S. Li, J. Qin, T. Gao, J. Du, K. Yuan, N. Li, L. Xu, J. Xu, Fabrication of Fe_3C nanoparticles embedded in N-doped carbon nanotubes/porous carbon 3D materials derived from distilled grains for high performance of potassium ion battery, J. Alloys Compd. 912 (2022) 165130.

[6] J. Lu, J. Liu, X. Gong, Z. Wang, Fe_3C doped modified nano-Si/C composites as high-coulombic-efficiency anodes for lithium-ion batteries, Sustain. Energ. Fuels 5 (2021) 6170-6180.

[7] T. Xiang, Z. Chen, Z. Rao, M. Yan, Z. Feng, X. Li, H. Yang, J. Huang, X. Shen, Hierarchical Fe/Fe_3C/C nanofibers as anodes for high capacity and rate in lithium-ion batteries, Ionics 27 (2021) 3663-3669.

[8] X. Zhao, D. Xia, J. Yue, S. Liu, In-situ generated nano-Fe_3C embedded into nitrogen-doped carbon for high performance anode in lithium-ion battery, Electrochimi. Acta 116 (2014) 292-299.

[9] C. Zhao, R. Fan, B. Murugesan, Y. Xu, J. Ma, J. Yao, I. Krucinska, Y. Cai, J. Gao, Uniformly inserted Fe_3C nanoparticles in sericin-derived hierarchical porous carbon for high-performance Li-ion battery, J. Alloys Compd. 881 (2021) 160661.

[10] D. Sun, M. Wang, Z. Li, G. Fan, L.-Z. Fan, A. Zhou, Two-dimensional Ti_3C_2 as anode material for Li-ion batteries, Electrochem. Commun. 47 (2014) 80-83.

[11] D. Qiu, B. Zhang, T. Zhang, T. Shen, Z. Fang, W. Zhao, J. Xu, Y. Hou, Flexible Co_9S_8-Carbon Nanofibers Architecture for Lithium-Ion Batteries: A Comprehensive Study of the Nature of Lithium Storage, ACS Materials Lett. 5 (2023) 1488-1496.

[12] D. Seo, M.R. Kim, J. Kyu Song, E. Kim, J. Koo, K.C. Kim, H. Han, Y. Lee, C. Won Ahn, Hollow Ti_3C_2 MXene/Carbon Nanofibers as an Advanced Anode Material for Lithium-Ion Batteries, ChemElectroChem 9 (2022) e202101344.

[13] Y. Guo, D. Zhang, Z. Bai, Y. Yang, Y. Wang, J. Cheng, P.K. Chu, Y. Luo, MXene nanofibers confining MnO_x nanoparticles: a flexible anode for high-speed lithium-ion storage networks, Dalton T. 51 (2022) 1423-1433.

[14] Y. Guo, D. Zhang, Y. Yang, Y. Wang, Z. Bai, P.K. Chu, Y. Luo, MXene-encapsulated hollow Fe_3O_4 nanochains embedded in N-doped carbon nanofibers with dual electronic pathways as flexible anodes for high-performance Li-ion batteries, Nanoscale 13 (2021) 4624-4633.

[15] L. Xie, J. Bi, X. Gao, L. Meng, C. Liu, J. Rong, Preparation of hollow core-shell structured Ti_3C_2@Ti_2SnC/CNFs with stable electrochemical performance as anode material for lithium ion battery, Ceram. Int. 49 (2023) 23003-23010.